1   REVISION 3

2

3   **Title:** Experimental investigation of $FeCO_3$ (siderite) stability in Earth's lower mantle

4   using XANES spectroscopy.

5

6   **Authors and affiliation:**

7   Valerio Cerantola[1,2*], Max Wilke[3], Innokenty Kantor[4], Leyla Ismailova[5], Ilya

8   Kupenko[6], Catherine McCammon[2], Sakura Pascarelli[1] and Leonid S. Dubrovinsky[2]

9

10   [1] European Synchrotron Radiation Facility, 71 Avenue des Martyrs, 38000 Grenoble,

11   FRANCE

12   [2] Bayerisches Geoinstitut, Universitat Bayreuth, Universitätsstraße 30, 95447

13   Bayreuth, GERMANY

14   [3] Institut für Erd- und Umweltwissenschaften, Universität Potsdam, Karl-Liebknecht-

15   Straße 24, 14476 Potsdam, GERMANY

16   [4] Danmarks Tekniske Universitet, Anker Engelunds Vej 1 Bygning 101A, 2800 Kgs.

17   Lyngby, DENMARK

18   [5] Skolkovo Innovation Center 143026, Nobel Stress 3, Moscow, RUSSIA

19   [6] Institut für Mineralogie, Universität Münster, Schlossplatz 2, 48149 Münster,

20   GERMANY

21

22   **Corresponding Author:** Valerio Cerantola, PhD valerio.cerantola@gmail.com

23

24   **Abstract**

25   We studied $FeCO_3$ using Fe K-edge X-ray absorption near-edge structure (XANES)

26   spectroscopy at pressures up to 54 GPa and temperatures above 2000 K. First-principles

27   calculations of Fe at the K-edge in $FeCO_3$ were performed to support the interpretation

28   of the XANES spectra. The variation of iron absorption edge features with pressure and

29   temperature in $FeCO_3$ matches well with recently reported observations on $FeCO_3$ at

30   extreme conditions, and provides new insight into the stability of Fe-carbonates in

31   Earth's mantle. Here we show that at conditions of the mid-lower mantle, ~50 GPa and

32   ~2200 K, $FeCO_3$ melts and partially decomposes to high-pressure Fe_3O_4. Carbon

33   (diamond) and oxygen are also inferred products of the reaction. We constrained the

34   thermodynamic phase boundary between crystalline $FeCO_3$ and melt to be at 51(1) GPa

1

35   and ~1850 K. We observe that at 54(1) GPa, temperature-induced spin crossover of

36   Fe^{2+} takes place from low to high spin such that at 1735(100) K, all iron in $FeCO_3$ is in

37   the high-spin state. A comparison between experiment and theory provides a more

38   detailed understanding of $FeCO_3$ decomposition observed in X-ray absorption spectra

39   and helps to explain spectral changes due to pressure-induced spin crossover in $FeCO_3$

40   at ambient temperature.

41   **Keywords**: deep carbon cycle, siderite, decomposition, melting, spin transition

42

43   **Introduction**

44   Subduction zones are descending limbs of Earth's lithosphere that, together

45   with ascending mantle plumes, are part of the active geodynamics of Earth that

46   influence its physical and chemical evolution (e.g. Tackley et al. 1993; Zhao 2003;

47   Walter et al. 2011; Chang et al. 2016). Subduction zones are Earth's largest recycling

48   system. They deliver crustal material to Earth's interior, where re-equilibration with the

49   surrounding mantle takes place mainly via complex physical mechanisms and chemical

50   reactions (e.g. Saunders and Tarney 1984; Keppler 1996; Motti et al. 2004; Bebout

51   2014). Material that is not recycled in the upper few hundred kilometers of subduction

52   zones will subduct deeper, ultimately towards the core-mantle boundary (CMB), where

53   different temperatures, pressures and oxygen fugacities (fO_2) govern the stability of

54   subducted material (e.g. Bina and Helffrich 1994; Dubrovinsky et al. 2003;

55   McCammon C. 2005; Rohrbach and Schmidt 2011; Stagno et al. 2013; Bykova et al.

56   2016). The general structure of subducting slabs is well known, and can be summarized

57   as a layered sequence of sedimentary rocks, oceanic crust and altered peridotite. The

58   fate of slabs exposed to the extreme conditions present in Earth's interior is already

59   understood in a general way. However, a more detailed understanding requires

60   investigation of the stability of each subducted phase in order to constrain the physics

61   and chemistry of subducting plates at different depths inside Earth.

62   Carbonates are one of the major components of the sedimentary layers (Rea and

63   Ruff 1996). Their presence inside Earth is supported by laboratory experiments (Stagno

64   et al. 2011; Liu et al. 2015; Cerantola et al. 2017) and through observations of natural

65   samples, for example inclusions in diamonds from the upper and lower mantle (e.g

66   Kvasnytsya and Wirth 2009; Kaminsky 2012; Kaminsky et al. 2016).

67   The three major carbonate components in the crust and upper mantle are $CaCO_3$

68   (calcite), $MgCO_3$ (magnesite), and $FeCO_3$ (siderite). Their presence in subducting

2

69   plates (Rea and Ruff, 1996) and recycled banded iron formations (Klein 2005;
70   Konhauser et al. 2017), and their stability in experiments that simulate the paragenesis
71   of carbonated eclogites (i.e. Kiseeva et al. 2012; Kiseeva et al. 2013) suggest that they
72   are the major source of carbon influx into the deep Earth.

73   Previous high-pressure studies on the carbonate endmembers $CaCO_3$, $MgCO_3$,
74   and $FeCO_3$ revealed high-pressure phase transitions in all three phases (i.e. Isshiki et
75   al. 2004; Ono et al. 2005; Lavina et al. 2009; Boulard et al. 2012; Smith et al. 2018; Li
76   et al. 2018), as well as in solid solutions between these phases (i.e. Liu et al. 2015; Mao
77   et al. 2011; Merlini et al. 2012; Solomatova and Asimow 2017). In particular, iron plays
78   a fundamental role in the behavior of carbonates at extreme conditions (e.g. Boulard et
79   al. 2012; Liu et al. 2015). Iron can radically change the thermodynamic stability of
80   carbonates, preserving them from breaking down at pressures and temperatures of the
81   lower mantle. This behavior may be a direct consequence of pressure-induced
82   electronic spin crossover (Lavina et al. 2009; Lobanov et al. 2015; Cerantola et al. 2015;
83   Lin et al. 2012), which was reported at ~43 GPa and room temperature for the
84   endmember $FeCO_3$, increasing to above 50 GPa at ~1200 K (Liu et al. 2014).

85   During subduction the majority of slab geotherms intersect a deep depression
86   along the melting curve of carbonated oceanic crust at depths of approximately 300 to
87   700 km (Thomson et al. 2015). $FeCO_3$ melting in the mantle has also been confirmed
88   by other experimental studies (Tao et al. 2013; Kang et al. 2015) that investigated its
89   stability from ambient conditions up to 20 GPa and ~2150 K. At pressures below ~6.8
90   GPa, $FeCO_3$ does not melt but decomposes through an auto redox dissociation reaction
91   to Fe_3O_4, a carbon polymorph and CO_2 (Tao et al. 2013; Kang et al. 2015). At pressures
92   above ~6.8 GPa $FeCO_3$ melts, with a minor quenched Fe^{3+}-rich phase interpreted to be
93   the result of redox dissociation of $FeCO_3$-liquid, leading to dissolved Fe^{3+} and CO_2 in
94   the carbonate melt (Kang et al. 2015). At P > 33 GPa, however, non-molecular CO_2
95   does not melt but dissociates to carbon and oxygen, which indicates that $FeCO_3$ melting
96   at lower mantle conditions produces Fe-oxides + C (diamond) + O_2 in the melt rather
97   than Fe-oxides + molecular CO_2 (Litasov et al. 2011). It is likely, however, that O_2 in
98   natural settings reacts further to form other phases, i.e. bonding with available cations
99   as a network former or modifier in the melt or forming stable crystalline phases such
100   as oxides. Cerantola et al. (2017) recently showed that $FeCO_3$ melting extends up to
101   ~70 GPa, where the transformation of $FeCO_3$ to high-pressure carbonate (HP-

3

102　carbonate) structures (CO_4^{4-} groups) begins (Oganov et al. 2008; Boulard et al. 2011;

103　Boulard et al. 2012; Merlini et al. 2015; Boulard et al. 2015; Cerantola et al. 2017;

104　Merlini et al. 2017). In the same work, Cerantola et al. (2017) unambiguously showed

105　that, after melting, $FeCO_3$ partially recrystallizes as α-Fe_2O_3 (hematite) and HP-Fe_3O_4

106　(Bykova et al. 2016) at pressures below and above 25 GPa, respectively. As

107　subproducts of the reactions the presence of other Fe-oxides (minor phases) and

108　diamond was observed (Cerantola et al. 2017). The change in redox state of the system

109　is likely caused by the stabilization of HP-Fe_3O_4 above 25 GPa (Dubrovinsky et al.

110　2003; Bykova et al. 2016). The kinetics of decomposition upon melting is still under

111　debate and will not be discussed here.

112　　　　In this study, we performed an experimental and theoretical investigation on the

113　high-pressure high-temperature behaviour of synthetic $FeCO_3$ using X-ray Absorption

114　Near-Edge Structure (XANES) spectroscopy at the Fe K-edge. Experimental

115　conditions covered pressures and temperatures down to the shallow-mid lower mantle

116　and XANES data complement X-ray diffraction studies of $FeCO_3$ stability in Earth's

117　mantle. In particular, XANES spectroscopy in dispersive mode is an extremely

118　powerful experimental technique capable of detecting decomposition and phase

119　transformation reactions on a millisecond time scale through the characteristic XANES

120　features of the material. We acknowledge, however, the limitation of XANES in phase

121　identification, for which other complementary techniques should be involved. In

122　parallel, major advances in *ab initio* modeling techniques enable calculation of *l*-

123　projected density of states, even in complex systems such as transition-metal oxides, in

124　order to obtain theoretical simulations of the absorption spectra beyond the multiple

125　scattering formalism (Joly 2001). The theoretical work complements our experimental

126　findings in qualitatively reproducing the observed spectral features. Discussion of

127　results focuses on two issues: a) the effect of extreme conditions on $FeCO_3$ absorption

128　spectra, and b) comparison between observed and calculated XANES spectra with

129　focus on $FeCO_3$ spin crossover. Finally we extend discussion of our experimental

130　observations to Earth's interior, and relate their importance to the fate of carbonates

131　within the dynamics of subduction zones.

132

133　**Methodology**

134　**Sample synthesis**

4

135   Single crystals of $^{57}FeCO_3$ were grown from $^{57}FeCO_3$ powder at 18 GPa and

136   1600 °C in a 1,200-t Sumitomo press at Bayerisches Geoinstitut (Bayreuth, Germany).

137     $FeCO_3$ powder was synthesized using ^{57}Fe-oxalate ($^{57}FeC_2O_4$) as precursor, which in

138   turn was obtained via chemical reactions starting from ^{57}Fe-metal (see Cerantola et al.

139   2015 for more details). Single crystals with an average size of $0.015 \times 0.015 \times$

140     $0.010\,mm^3$ were loaded together with small ruby chips 5 to 10 μm in diameter (for

141   pressure estimation) into BX90-type diamond anvil cells (DACs) (Kantor et al. 2012)

142   and high-pressure membrane cells from the European Synchrotron Radiation Facility

143   (ESRF). The Dewaele et al. (2008) pressure scale was used to estimate pressure from

144   the fluorescence line of the ruby spheres. Diamonds with culet sizes of 250 μm and

145   rhenium gaskets with 120 μm starting diameter holes were employed in all experiments.

146   Neon was used as a pressure-transmitting medium and loaded at Bayerisches

147   Geoinstitut (Kurnosov et al. 2008) and/or ESRF. High temperatures were achieved

148   using the double-sided YAG laser heating system at the ID24 beamline at ESRF.

149   Temperature uncertainties (error bars) were estimated using the difference between the

150   measured temperature from the upstream and downstream sides of the double-sided

151   laser heating system. To test for pressure gradients, in some experiments we placed two

152   to three ruby chips in different positions inside the pressure chamber. In all cases

153   pressure differences measured by different ruby spheres loaded in the same gasket

154   chamber were not more than 1 GPa along the entire pressure range investigated (up to

155   54 GPa).

156

157   **XANES spectroscopy**

158   Fe K-edge XANES measurements were performed at ESRF at the energy

159   dispersive X-ray absorption spectroscopy (XAS) beamline ID24 (e.g. Pascarelli et al.

160   2016). The beam was focused horizontally using a curved polychromator Si 111 crystal

161   in Bragg geometry and vertically with a bent Si mirror. The obtained cross-section at

162   the full width half maximum (FWHM) is about 3 x 5 $μm^2$ in horizontal and vertical

163   directions, respectively. The Bragg diffraction peaks arising from the diamond anvils

164   were removed from the energy range of interest by changing the orientation of the DAC

165   and following in real time the intensity of the transmitted beam on a two-dimensional

166   detector. The measured XANES spectra were normalized using the Athena software

167   package (Ravel et al. 2005), and the second-order polynomial for the pixel to energy

168   conversion parameters was calibrated using a reference α-Fe foil spectrum.

5

169

170   *Ab initio* calculations

171   Theoretical XANES calculations were performed using the FDMNES code (Joly

172   2001; Bunau and Joly 2009). In FDMNES, the Schrödinger equation is solved by the

173   finite difference method (FDM) within the local density approximation. For calculation

174   of the spectra, structural models of $FeCO_3$ and $HP-Fe_3O_4$ were used that were based on

175   high-pressure single-crystal X-ray diffraction (SCXD) data measured on a single

176   crystal of $FeCO_3$ from the same synthesis run used to produce the samples for XANES

177   (Table 1). SXRD measurements were carried out at the high-pressure X-ray diffraction

178   beamline ID09a (now ID15b) at the ESRF (MAR555 detector, λ=0.4126 Å). A $FeCO_3$

179   single crystal with average size $0.015 \times 0.015 \times 0.010$ mm^3 was loaded and compressed

180   to different pressures in a standard ESRF membrane cell using neon as a quasi-

181   hydrostatic pressure medium. X-ray diffraction images were collected during

182   continuous rotation of DACs typically from −38° to +38° on ω; while data collection

183   experiments were performed by narrow 0.5–1° scanning of the same ω range. Typical

184   images and integrated XRD patterns are illustrated in Cerantola et al. (2017) who

185   collected comparable data on similar samples. Indexing and refinement of the unit cell

186   parameters was performed using CrysAlisPro software (Agilent Technologies Ltd.

187   2014), and the complete procedure for data analysis is described in Cerantola et al.

188   (2017).

189   The cluster radius for the calculations was set to 6 Å and was checked for

190   convergence beforehand. The electron density of the potential was optimized in a self-

191   consistent manner using the same cluster size. Calculations included quadrupolar

192   transitions. The natural core-hole broadening of 1.4 eV was used and the value of the

193   Fermi energy set to include excitations to d-states in the pre-edge region. Finally,

194   calculated spectra were shifted in energy to match the experimental ones. Vibrational

195   disorder from finite temperature was not included.

196

197   **Results**

198   **$FeCO_3$ stability as a function of pressure and temperature**

199   The temperature effect on $FeCO_3$ stability at 36(1) GPa observed by XANES

200   spectroscopy is shown in Figure 1. At room temperature before heating, a typical

201    $FeCO_3$ XANES spectrum is observed with iron in the high-spin state, showing a weak

202   pre-edge peak at 7112 eV and two main peaks, identified in the figures as "1" and "2"

6

203 (Wilke et al. 2001; Cerantola et al. 2015). Heating the sample to 1890(100) K causes a

204 decrease in the intensity of peak 2 and a smoothing of the EXAFS oscillations above

205 7160 eV. Upon further heating at 2270(200) K the spectrum radically changes,

206 manifested by the loss of the double-peak structure at the main edge and the appearance

207 of a new peak at 7113.5 eV. New features at 7155, 7173 and 7210 eV appear, drastically

208 modifying the beginning of the EXAFS region. The flattening of the spectrum is a clear

209 consequence of high temperature, and suggests complete or at least partial melting of

210 the sample (e.g. Aquilani et al. 2015). The spectrum after quench shows identical

211 features to the high temperature spectrum, but more pronounced due to the absence of

212 thermal damping.

213 Representative XANES spectra of $FeCO_3$ at 51(1) GPa and increasing

214 temperature are plotted in Figure 2. In particular, Figure 2a shows low-spin $FeCO_3$ at

215 room temperature with the characteristic pre-edge at 7112 eV and an additional feature

216 at 7116.5 eV. Peak 2 is more intense than peak 1 and a pronounced hump is observed

217 at 7155 eV (feature 3, Cerantola et al. 2015). The temperature effect is evident at

218 1600(100) K and 1775(100) K, where an exchange of intensity between peaks 1 and 2

219 and a smoothing of the first EXAFS oscillation are observed. However, despite the high

220 temperature, the characteristic pre-edge peak position at 7112 eV is preserved. Heating

221 to 1890(100) K and higher completely changes the spectral shape. The maximum of the

222 pre-edge shifts from 7112 eV to 7113.5 eV (Fig. 3), and peak 1 shifts to slightly higher

223 energies and "merges" with peak 2, the latter becoming rather a weak "hump" of the

224 first peak. The ambient temperature spectrum after quenching from 2025(100) K (Fig.

225 2a, top) preserves the same features observed at high temperature, but they appear

226 sharper due to the absence of heating.

227 After quenching, the same sample was re-annealed up to 1830(100) K. Annealing

228 at lower temperature caused partial recrystallization of low-spin (LS) $FeCO_3$ as seen by

229 the increase in intensity of peak 2 (Cerantola et al. 2015) up to 1675(100) K and a

230 change in spectral shape at 1830(100) K. The XANES region of the room temperature

231 spectrum after annealing (Fig. 2b, top) is similar to the one before heating (Fig. 2a,

232 bottom) and is characterized by distinctive peaks marked "1", "2" and "3" in the

233 spectra. The EXAFS region, however, is clearly different at about 7200 eV, displaying

234 two new humps at ~7185 and ~7210 eV that are both absent in the $FeCO_3$ spectrum

235 before heating (Fig. 2a, bottom).

236   The evolution of the XANES spectrum of low-spin $FeCO_3$ at 54(1) GPa and

237   moderate temperature is shown in Figure 4. Peak 2, which is the most intense feature

238   in the spectrum at ambient temperature, becomes progressively less intense upon

239   heating, while peak 1 becomes the dominant peak at 1735(100) and 1840(100) K.

240   Moreover, high temperature causes the loss of peak 3 and the disappearance of the pre-

241   edge peak at 7116.5 eV. Similar to Figures 1 and 2, high temperature tends to flatten

242   the spectra, especially in the EXAFS region, where the characteristic features become

243   smoother and less pronounced. Note that the room temperature spectrum after

244   quenching matches the spectrum before heating extremely well.

245

246   **XANES spectra calculated below and above spin crossover**

247    $FeCO_3$ exhibits space-group symmetry R-3c (calcite-group rhombohedral

248   carbonates), where in the hexagonal setting, iron is located at the cell origin (6b),

249   oxygen is at x, 0, 1/4 (18e), and carbon is at 0, 0, 1/4 (6a) (Bragg 1913). The atomic

250   arrangement can be envisioned as a distorted rocksalt structure with Fe^{2+} as the cation

251   and CO_3^{2-} groups as the anions. The CO_3^{2-} groups form planes perpendicular to the *c*

252   axis with Fe occupying the interstitial octahedral voids between the planes. No bond or

253   polyhedral edge is parallel to the *c* axis.

254   We calculated XANES spectra of $FeCO_3$ by *ab initio* simulation using the

255   structural lattice parameters measured by SXRD at 4, 37, and 55 GPa at ambient

256   temperature (Fig. 5, Table 1). Qualitatively the features of the experimental spectra are

257   reproduced well by the calculations: a) both experimental and calculated spectra are

258   characterized by two main peaks (identified as "1" and "2") that shift to higher energies

259   with increasing pressure, b) their relative intensities also change similarly with

260   increasing pressure, such that at 55 GPa, peak 2 is more intense than peak 1 (Fig. 5),

261   and c) the pre-edge feature observed at 7117 eV in the simulated spectra at 37 and 55

262   GPa coincides with the pre-edge feature at 7116.5 eV of the experimental spectra at

263   similar pressures. There are some differences, however: a) the pre-edge peak at 7112

264   eV in the experimental spectra (black) is not well represented in the calculated spectra

265   (red), where instead two strong pre-edges are observed at 7115 and 7117 eV (Figs. 5a,

266   5b and 5c), and b) spectra calculated at 37 and 55 GPa are characterized by a dip at

267   7125 eV visible on the left side of peak 1 that becomes sharper with pressure, but this

268   feature is nonexistent in the experimental spectra, which instead display a hump at 7155

269   eV (peak 3) that is completely absent in the simulations.

8

270

Discussion

FeCO$_3$ melting

273   In a recent study, Cerantola et al. (2017) investigated the stability of FeCO$_3$ up to
274   110 GPa and T > 2500 K using SXRD and energy-domain synchrotron Mössbauer
275   source (SMS) spectroscopy. At the conditions relevant for this study, P > 36 GPa and
276   T > 1850 K, FeCO$_3$ melts, partially dissociating to HP-Fe$_3$O$_4$, diamond and oxygen (i.e.
277   Litasov et al. 2011). The presence of other Fe-oxide phases cannot be excluded
278   (Cerantola et al. 2017). Electron microprobe analyses (EMPA) (Tao et al. 2013, Kang
279   et al. 2015), SXRD and Mössbauer spectroscopy (Cerantola et al. 2017) confirmed that
280   even after prolonged heating the decomposition is never complete, and after quenching
281   the presence of recrystallized FeCO$_3$ and HP-Fe$_3$O$_4$ is always observed. Note that,
282   incomplete decomposition could be caused by pressure and temperature gradients in
283   the DAC, however we believe this is not the case since similar behavior was observed
284   in several studies from different authors and using various experimental techniques,
285   such as DACs and multi-anvils apparatus (Tao et al., 2013, Kang et al. 2015, Cerantola
286   et al. 2017).

287   The experimental results of the present study are consistent with Cerantola et al.
288   (2017) (Fig. 6). At 36(1) GPa, temperatures higher than 1890(100) K (the last
289   temperature where FeCO$_3$ XANES features were clearly observed, Fig. 1) cause a
290   drastic change to the spectrum, which is interpreted to indicate complete or partial
291   melting of FeCO$_3$. Previous work has shown that melting is not stoichiometric due to
292   partial redox dissociation of liquid FeCO$_3$, leading to dissolved Fe^{3+} and CO$_2$ in the
293   carbonate melt below ~33 GPa, whereas above ~33 GPa the carbonate melt
294   recrystallizes after quenching as FeCO$_3$, HP-Fe$_3$O$_4$, C (diamond) and O$_2$ (Litasov et al.
295   2011; Kang et al. 2015; Cerantola et al. 2017). A similar case is observed at 51(1) GPa
296   and temperatures up to ~2000 K (Fig. 2). The intensity exchange between peaks 1 and
297   2 at 1600(100) and 1775(150) K is evident (Fig. 2), which is caused by the low- to high-
298   spin transition of Fe^{2+} (Liu et al. 2014; Liu et al. 2015; Cerantola et al. 2015). The
299   characteristic pre-edge peak position at 7112 eV and the position of peaks 1 and 2
300   clearly indicate that at these conditions, FeCO$_3$ is stable and no decomposition has taken
301   place. In contrast, the spectra at higher temperatures (collected above 1890(100) K)
302   show a collapse of the FeCO$_3$ characteristic features, the most evident change being in
303   the pre-edge which shifts from 7112 to 7113.5 eV (Fig. 3). Again, the observed changes

9

304   are inferred to be caused by non-stoichiometric recrystallization due to a self-oxidation

305   reaction during melting with the consequent formation of HP-Fe_3O_4 (Kang et al. 2015;

306   Cerantola et al. 2017).

307   Interestingly, annealing the sample at moderate temperatures between 1610(100)

308   and 1675(100) K caused the back reaction to occur, where partial recrystallization of

309   LS-$FeCO_3$ from a mixture of HP-Fe_3O_4, C (diamond) + O_2 is observed (Fig. 2b). We

310   suspect the presence of HP-Fe_3O_4 and possibly other Fe-oxide phases due to two humps

311   at ~7185 and ~7210 eV in the spectra of recrystallized samples that are absent in the

312   initial LS-$FeCO_3$ spectrum before heating (Fig. 2a). At 51(1) GPa, the changes in the

313   spectra caused by heating below 1830(100) K and above 1890(100) K allow us to locate

314   the thermodynamic phase boundary between crystalline $FeCO_3$ and melt at about 1850

315   K. Results of the experiment performed at 54(1) GPa and high temperature are

316   consistent with this conclusion (Fig. 4).

317   In order to verify our experimental observations, we simulated the XANES

318   spectrum of HP-Fe_3O_4 at 51 GPa using structural data from Table 1. Figure 7a shows

319   the calculated spectra of HP-Fe_3O_4 at 51 GPa (blue) and LS-$FeCO_3$ at 55 GPa (black).

320   To our knowledge there are no experimental XANES spectra of pure HP-Fe_3O_4 in the

321   literature. The calculated $FeCO_3$ spectrum matches well with the experimental one at

322   energies above the absorption edge (see also Fig. 5). Figure 7b shows the experimental

323   XANES spectrum of $FeCO_3$ obtained after laser heating at 51(1) GPa and 2025(100) K

324   and the sum of the calculated spectra for LS-$FeCO_3$ at 55 GPa and HP-Fe_3O_4 at 51 GPa.

325   The similarities are evident: a) peak 1 is more intense than peak 2, and b) both peaks in

326   calculated and experimental spectra are located at the same energy position. The

327   calculated spectrum also shows a third peak (peak 3), that is clearly not present in the

328   experimental spectrum. However, it is difficult to estimate the relative abundance for

329   each component, which can affect the spectral shape. We estimated a run product

330   containing 50 wt% HP-Fe_3O_4 and 50 wt% LS-$FeCO_3$, but the actual amount of each

331   phase is not known. The difference in the pre-edge region can be explained by the

332   inability of the code to simulate this feature, because the pre-edge represents

333   quadrupolar excitations to localized states.

334   The updated $FeCO_3$ stability diagram based on XANES data (Fig. 6) is largely

335   consistent with the $FeCO_3$ stability fields reported by Cerantola et al. (2017). One slight

336   difference is the position of the melting curve, which is around 200 K lower at its

337   highest point in the updated version compared to the original diagram. While this

338   difference is largely within the uncertainties of the temperature measurements, we note

339   that XANES spectroscopy in dispersive mode is capable of detecting reactions on a

340   millisecond time scale and hence the *in situ* measurements in the present study may

341   provide a more accurate determination of melting compared to studies on quenched

342   samples.

343

344   **Spin crossover features from simulated spectra**

345   Cerantola et al. (2015) first reported spin crossover in $FeCO_3$ observed by

346   XANES. Here, we compare experimental data with *ab initio* simulations of XANES

347   spectra using the onset of the edge and the first EXAFS maximum. The similarity

348   between simulated and experimental spectra is quite remarkable (Fig. 5), which can be

349   attributed to the fact that the FDMNES code overcomes limitations from the Muffin

350   Tin Approximation (Rehr and Albers 2000). In particular, the double peak feature at

351   the main edge (peaks 1 and 2) has been reproduced, which is the one most indicative

352   for the change in Fe spin state. The changes in the spectra, the broadening of the peaks,

353   and their shift to higher energies with pressure are related to changes in the electronic

354   structure due to shortening of Fe-O distances. The shortening is also directly seen from

355   the shift of the first EXAFS maximum between 7170 and 7190 eV to higher energy

356   ($\sim$20 eV), which may be described by the relation ΔE x R^2 = const. (e.g. Bianconi et al.

357   1983; Wilke et al. 2007), where ΔE is the energy difference between the onset of the

358   edge and the first EXAFS maximum and R is the Fe-O distance.

359   The pre-edge region at 7112 eV in the experimental spectra and at 7115 eV in the

360   simulated spectra is related to localized *1s* $\rightarrow$ *3d* transitions, which are quadrupolar in

361   nature and only become dipole-allowed through hybridization of *p* and *d* orbitals for

362   non-centro-symmetric sites. In theory, the pre-edge represents a region of the spectrum

363   that is sensitive to changes in Fe spin as shown by Westre et al. (1997). Simulated

364   spectra do show slight differences in this energy region between high-spin and low-

365   spin state; however a comparison with experimental spectra is difficult due to low

366   resolution and low statistical quality of the data in this region. The feature at 7116.5

367   eV, which emerges in the experimental spectra at and above spin crossover, is likely

368   related to excitations of 1s to 4p electron states of the valence band (e.g., Caliebe et al.

369   1997). This feature becomes better resolved at higher pressures because the main edge

370   shifts to higher energy due to decreasing Fe-O distance. In the simulations this feature

371   is also at $\sim$7117 eV and becomes better resolved due to the shift of the main edge to

11

372   higher energy, similar to experiment. Likewise, the depression at around 7125 eV

373   present in the simulated spectrum at 37 and 55 GPa is also related to the shortening of

374   the Fe-O distance upon compression and spin crossover, so that the feature is more

375   pronounced and sharper at 55 GPa than at 37 GPa due to the shift of the main edge. At

376   higher energy, the presence of the hump at ~7155 eV (feature 3) in the experimental

377   spectra above 37 GPa is not observed in the simulations, which suggests that this feature

378   stems from multiple scattering and cannot be adequately reproduced by the calculation

379   performed here (Fig. 5). Overall, the theoretical spectra and analysis of the l-projected

380   density of states show that the changes in the main-edge XANES region of the spectra

381   are mainly related to the shift of p-states to higher energies, which is induced by the

382   reduction of the Fe-O distance.

383   Methods for *ab initio* simulation of XANES spectra still have shortcomings when

384   compared to experiments (Rehr and Albers 2000; Joly 2001; Bunau and Joly 2009).

385   Interactions of the photoelectron with electronic states of the host close to the edge are

386   quite complex and thus the fine structure cannot always be fully replicated. In

387   particular, excitations to localized states are known to be less well described by real-

388   space calculations, particularly if they are quadrupolar in nature. Furthermore, the core-

389   hole screening is only approximated. This may substantially shift or suppress features

390   in the calculated spectrum. Finally, these calculations did not include effects caused by

391   thermal disorder to avoid broadening of observed features that were the main focus of

392   our study.

393

394   **Implications**

395   Carbonate-bearing subducting slabs have different thermal profiles, which

396   mainly vary based on slab age and velocity of subduction. Colder slabs subduct faster

397   mainly due to their enhanced density (e.g. Syracuse et al. 2010). Recently, it has been

398   proposed that the majority of slab geotherms intersect a deep depression along the

399   melting curve of carbonated oceanic crust at depths of approximately 300 to 700 km

400   during subduction (Thomson et al. 2015). At those depths, $FeCO_3$ melts, forming α-

401   Fe_2O_3 below ~25 GPa (Kang et al. 2015; Cerantola et al. 2017) and HP-Fe_3O_4 at higher

402   pressure (depths below 750 km) (Cerantola et al. 2017). These redox dissociations are

403   accompanied by the formation of other compounds such as diamond, oxygen and

404   possibly Fe-oxides with different stoichiometry. $FeCO_3$ incongruent melting has

405   important implications for the influx of carbon via Fe-carbonates inside Earth, because

12

406   it provides a mechanism for $FeCO_3$ to partly survive even in subducting plates with

407   higher thermal regimes, which promotes subduction to the deepest regions of Earth's

408   mantle. For instance, $FeCO_3$-rich carbonated liquids that escape from subducting plates

409   can recrystallize to solid $FeCO_3$ in proximity of colder regions in the lower mantle,

410   stagnating there and being subject of deep Earth's geodynamic phenomena, such us

411   further downwelling or upwelling.

412   In this study we investigated the melting of $FeCO_3$ at high pressure and high

413   temperature. Based on our results, we suggest that subducting slabs with average

414   surface temperature (~1250 K at 15 GPa; Syracuse et al. 2010) will undergo carbonate-

415   melting processes (Thomson et al. 2016) that result in partial $FeCO_3$ decomposition to

416   oxides and diamond. In contrast, subducting slabs with lower surface temperature

417   (~1050 K at 15 GPa; Syracuse et al. 2010 or 1500 K at 70 GPa; e.g. Kaneshima and

418   Helffrich 2003; Komabayashi et al. 2009) could survive subduction through Earth's

419   mantle without undergoing melting until pressures and temperatures were high enough

420   to cause transformation of CO_3^{2-}-carbonates to their high-pressure structures

421   characterized by CO_4^{4-} tetrahedra above 70 GPa (Cerantola et al. 2017; Merlini et al.

422   2015; Merlini et al. 2017).

423

433

434   **References**

435

436   Aquilani, G., Trapananti, A., Karandikar, A., Kantor, I., Marini, C., Mathon, O.,

437   Pascarelli, S., and Boehler, R. (2015) Melting of iron determined by X-ray absorption

438   spectroscopy to 100 GPa. Proceedings of the National Academy of Science, 112,

439   12042–12045.

13

440

441   Bebout, G.E. (2014) Metamorphic chemical geodynamics of subduction zones. Earth

442   and Planetary Science Letters, 260, 373–393.

443

444   Bianconi, A., Dell'Ariccia, M., Gargano, A., and Natoli, C.R. (1983) Bond length

445   determination using XANES. In A. Bianconi, L. Incoccia, and S. Stilpcich, Eds.,

446   EXAFS and Near Edge Structure, 27, p. 57-61. Springer Series in Chemistry and

447   Physics, Berlin.

448

449   Bina, C.R. and Helffrich, G. (1994) Phase transition Clapeyron slopes and transition

450   zone seismic discontinuity topography. Journal of Geophysical Research, 99, 853-860.

451

452   Boulard, E., Gloter, A., Corgne, A., Antonangeli, D., Auzende, A-L., Perrillat, J-P.,

453   Guyot, F., and Fiquet, G. (2011) New host for carbon in the deep Earth. Proceedings of

454   the National Academy of Science, 108, 5184–5187.

455

456   Boulard, E., Menguy, N., Auzende, A.L., Benzerara, K., Bureau, H., Antonangeli, D.,

457   Corgne, A., Morard, G., Siebert, J., Perrillat, J.P., Guyot, F., and Fiquet, G. (2012)

458   Experimental investigation of the stability of Fe-rich carbonates in the lower mantle.

459   Journal of Geophysical Research, 117, B02208.

460

461   Boulard, E., Pan, D., Galli, G., Liu, Z., and Mao, W. (2015) Tetrahedrally coordinated

462   carbonates in Earth's lower mantle. Nature Communications, 6, 631.

463

464   Bragg, W.L. (1913) The Structure of Some Crystals as Indicated by Their Diffraction

465   of X-rays. Proceedings of the Royal Society A, London 89, 248.

466

467   Bunau, O., and Joly, Y. (2009) Self-consistent aspects of x-ray absorption calculations.

468   Journal of Physics: Condensed Matter, 21, 34.

469

470   Bykova, E., Dubrovinsky, L., Dubrovinskaia, N., Bykov, M., McCammon, C.,

471   Ovsyannikov, S.V., Liermann, H-P., Kupenko, I., Chumakov, A.I., Rueffer, R.,

472   Hanfland, M., and Prakapenka, V. (2016) Structural complexity of simple Fe_2O_3 at high

473   pressures and temperatures. Nature Communications, 7, 10661.

14

474

475   Caliebe, W.A., Kao, C.C., Hastings, J.B., Taguchi, M., Kotani, A., Uozumi, T., and de

476   Groot, F.M.F. (1998) 1s2p resonant inelastic x-ray scattering in γ-Fe$_2$O$_3$. Physical

477   Review B, 58, 13452-13458.

478

479   Cerantola, V., McCammon, C., Kupenko, I., Kantor, I., Marini, C., Wilke, M.,

480   Ismailova, L., Solopova, N., Chumakov, A.I., Pascarelli, S., and Dubrovinsky, L.

481   (2015) High-pressure spectroscopic study of siderite (FeCO$_3$) with focus on spin

482   crossover. American Mineralogist, 100, 2670-2681.

483

484   Cerantola, V., Bykova, E., Kupenko, I., Merlini, M., Ismailova, L., McCammon, C.,

485   Bykov, M., Chumakov, A., Petitgirard, S., Kantor, I., Svitlyk, V., Jacobs, J., Prescher,

486   C., Rüffer, R., and Dubrovisnky, L. (2017) Iron bearing carbonates stability in the deep

487   Earth's interior. Nature Communications, 8, 15960.

488

489   Chang, S-J., Ferreira A.MG. and Faccenda, M. (2016) Upper- and mid-mantle

490   interaction between the Samoan plume and the Tonga–Kermadec slabs. Nature

491   Communications, 7, 10799.

492

493   CrysAlisPro Software system. Version 1.171.37.35 (2014). Agilent Technologies Ltd,

494   Yarnton, Oxfordshire, England.

495

496   Dubrovinsky, L.S., Dubrovinskaia, N.A. McCammon, C. Rozenber, G.Kh., Ahuja, R.

497   Osorio-Guillen, J.M, Dmitriev, V., Weber, H-P., Bihan, T.Le., and Johansson B. (2003)

498   The structure of the metallic high-pressure Fe$_3$O$_4$ polymorph: experimental and

499   theoretical study. Journal of Physics: Condensed Matter, 15, 45.

500

501   Isshiki, M., Irifune, T., Hirose, K., Ono, S., Ohishi, Y., Watanuki, T., Nishibori, E.,

502   Takata, M., and Sakata, M. (2004) Stability of magnesite and its high-pressure form in

503   the lowermost mantle. Nature, 427, 60-63.

504

505   Joly, Y. (2001) X-ray absorption near-edge structure calculations beyond the muffin-

506   tin approximation. Physical Review B, 63, 125120.

507

508   Li, X., Zhang, Z., Lin, J-F., Ni, H., Prakapenka, V., and Mao, Z. (2018) New High-
509   Pressure Phase of $CaCO_3$ at the Topmost Lower Mantle: Implication for the Deep-
510   Mantle Carbon Transportation. Geophysical Research Letters, 45, 1355-1360.

512   Litasov, K.D., Goncharov, A.F., and Hemley, R.J. (2011) Crossover from melting to
513   dissociation of CO_2 under pressure: Implications for the lower mantle. Earth and
514   Planetary Science Letters, 309, 318-323.

516   Kaminsky, F. (2012) Mineralogy of the lower mantle: A review of 'super-deep' mineral
517   inclusions in diamond. Earth and Planetary Science Letters, 110, 127-147.

519   Kaminsky, F.V., Ryabchikov, I.D. and Wirdth, R. (2016) A primary natrocarbonatitic
520   association in the Deep Earth. Mineralogy and Petrology, 110, 387-398, DOI
521   10.1007/s00710-015-0368-4.

523   Kaneshima, S., and Helffrich, .G (2003) Subparallel dipping heterogeneities in the mid-
524   lower   mantle.   Journal   of   Geophysical   Research,   108,   B5,   DOI:
525   10.1029/2001JB001596.

527   Kang, N., Schmidt, M.W., Poli, S., Franzolin, E., and Connolly, J.A.D. (2015) Melting
528   of siderite to 20 GPa and thermodynamic properties of $FeCO_3$-melt. Chemical Geology,
529   400, 34-43.

531   Kantor, I. Yu., Prakapenka, V., Kantor, A., Dera, P., Kurnosov, A., Sinogeikin, S.,
532   Dubrovinskaia, N., and Dubrovinsky, L. (2012) BX90: A new diamond anvil cell
533   design for X-ray diffraction and optical measurements. Review of Scientific
534   Instruments, 83, 125102.

536   Katsura, T., Yoneda, A., Yamazaki, D., Yoshino, T., and Ito, E. (2010) Adiabatic
537   temperature profile in the mantle. Physics of the Earth and Planetary Interiors, 183,
538   212-218.

540   Keppler, H.K. (1996) Constraints from partitioning experiments on the composition of
541   subduction-zone fluids. Nature, 380, 237-240.

542

543   Kiseeva, E. S., Yaxley, G. M., Hermann, J., Litasov, K. D., Rosenthal, A., Kamenetsky,

544   V. S. (2012) An experimental Study of Carbonated Eclogite at 3.5-5.5 GPa –

545   Implications for Silicate and Carbonate Metasomatism in the Cratonic Mantle. Journal

546   of Petrology, 53, 4, 727-759.

547

548   Kiseeva, E. S., Litasov, K. D., Yaxley, G. M., Ohtani, E., and Kamenetsky, V. S. (2013)

549   Melting and Phase Relations of Carbonated Eclogite at 9-21 GPa and the Petrogenesis

550   of Alkali-Rich Melts in the Deep Mantle. Journal of Petrology, 54, 8, 1555-1583.

551

552   Klein, C. (2005) Some Precambrian banded iron-formations (BIFs) from around the

553   world: Their age, geologic setting, mineralogy, metamorphism, geochemistry, and

554   origin. American Mineralogist, 90, 1473-1499.

555

556   Komabayashi, T., Omori, S., Hirose, K., and Maruyama, S. et al. (2009) On the slab

557   temperature in the deep lower mantle. AGU Sping Meeting Abstracts.

558

559   Konhauser, K. P., Planavsky, N. J., Hardisty, D. S., Robbins, L. J., Warchola, T. J.,

560   Haugaard, R., Lalonde, S. V., Partin, C. A., Oonk, P. B. H., Tsikos, H., Lyons, T. W.,

561   Bekker, A., and Johnson, C. M. (2017) Iron Formations: A global record of Neoarchean

562   to Palaeoproterozoic environmental history. Earth-Science Reviews, 172, 140-177.

563

564   Kurnosov, A., Kantor, I., Boffa-Ballaran, T., Lindhardt, S., Dubrovisnky, L.,

565   Kuznetsov, A., and Zehnder, B.H. (2008) A novel gas-loading system for mechanically

566   closing of various types of diamond anvil cells. Review of Scientific Instruments, 79,

567   045110.

568

569   Kvasnytsya, V.M., and Wirth, R. (2009) Nanoinclusions in microdiamonds from

570   Neogenic sands of the Ukraine (Samotkan' Placer); a TEM study. Lithos, 113, 454-

571   464.

572

573   Lavina B., Dera P., Downs R.T., Prakapenka V., Rivers M., Sutton S., and Nicol M.

574   (2009) Siderite at lower mantle conditions and the effects of the pressure-induced spin-

575   pairing transition. Geophysical Research Letters, 36, L23306.

17

576

577   Lin, J.F., Liu, J., Jacobs, C., and Prakapenka, V.B. (2012) Vibrational and elastic
578   properties of ferromagnesite across the electronic spin-pairing transition of iron.
579   American Mineralogist, 97, 583-591.

580

581   Liu, J., Lin, J.F., Mao, Z., and Prakapenka, V.B. (2014) Thermal equation of state and
582   spin transition of magnesiosiderite at high pressure and temperature. American
583   Mineralogist, 99, 84-93.

584

585   Liu, J., Lin, J.-F., and Prakapenka, V.B. (2015) High-pressure orthorhombic
586   ferromagnesite as a potential deep-mantle carbon carrier. Scientific Reports, 5, 7640,
587   doi: 10.1038/srep07640.

588

589   Lobanov, S.S., Goncharov, A.F., and Litasov, K.D. (2015) Optical properties of siderite
590   ($FeCO_3$) across the spin transition: Crossover to iron-rich carbonates in the lower
591   mantle. American Mineralogist, 100, 1059-1064.

592

593   Mao, Z., Armentrout, M., Rainey, E., Manning, C.E., Dera, P., Prakapenka, V., and
594   Kavner, A. (2011) Dolomite III: A new candidate lower mantle carbonate. Geophysical
595   Research Letters, 38, L22303.

596

597   McCammon, C. (2005) The paradox of mantle redox. Science, 308, 807–808.

598

599   Merlini, M., Crichton, W.A., Hanfland, M., Gemmi, M., Mueller, H., Kupenko, I., and
600   Dubrovinsky, L. (2012) Structures of dolomite at ultrahigh pressure and their influence
601   on the deep carbon cycle. Proceedings of the National Academy of Science, 109,
602   13509-13514.

603

604   Merlini, M., Hanfland, M., Salamat, A., Petitgirard, S., and Müller, H. (2015) The
605   crystal structures of $Mg_2Fe_2C_4O_{13}$, with tetrahedrally coordinated carbon, and $Fe_{13}O_{19}$,
606   synthesized at deep mantle conditions. American Mineralogist, 100, 2001-2004.

607

608   Merlini, M., Cerantola, V., Gatta, D., Gemmi, M., Hanfland, M., Kupenko, I., Lotti, P.,
609   Müller, H. and Zhang, L. (2017) Dolomite-IV: Candidate structure for a carbonate in
610   the Earth's lower mantle. American Mineralogist, 102, 1763-1766.
611

612   Motti, M.J., Wheat, C.G., Fryer, P. Gharib, J. Martin, B.J. (2004) Chemistry of springs
613   across the Mariana forearc shows progressive devolatilization of the subducting plate.
614   Geochimica et Cosmochimica Acta, 68, 4915-4933.
615

616   Müller, J., Efthimiopoulos, I., Sandro, J., and Koch-Müller, M. (2017) Effect of
617   temperature on the pressure-induced spin transition in siderite and iron-bearing
618   magnesite: a Raman spectroscopy study. European Journal of Mineralogy, 29, 785-793.
619

620   Oganov, A.R., Ono, S., Ma, Y.M., Glass, C.W., and Garcia, A. (2008) Novel high-
621   pressure structures of $MgCO_3$, $CaCO_3$ and CO_2 and their role in earth's lower mantle.
622   Earth and Planetary Science Letters, 273, 38–47.
623

624   Ono, S., Kikegawa, T., Ohishi, Y., and Tsuchya, J. (2005) Post-aragonite phase
625   transformation in CaCO3 at 40 GPa. American Mineralogist, 90, 667-671.
626

627   Pascarelli, S., Mathon, O., Mairs, T., Kantor, I., Agostini, G., Strohm, C., Pasternak,
628   S., Perrin, F., Berruyer, G., Chappelet, P., Clavel, C. and Dominguez, M. C. (2016) The
629   Time-resolved and Extreme-conditions XAS (TEXAS) facility at the European
630   Synchrotron Radiation Facility: the energy-dispersive X-ray absorption spectroscopy
631   beamline ID24. Journal of Synchrotron Radiation, 23, 353-368.
632

633   Ravel, B., and Newville, M. (2005) ATHENA, ARTEMIS, HEPHAESTUS: data
634   analysis for X-ray absorption spectroscopy using IFEFFIT. Journal of synchrotron
635   radiation, 12, 537–41.
636

637   Rea, D.K., and Ruff, L.J. (1996) Composition and mass flux of sediment entering the
638   world's subduction zones: Implications for global sediment budgets, great earthquakes,
639   and volcanism. Earth and Planetary Science Letters, 140, 1-12.
640

641   Rehr, J.J., and Albers, R.C. (2000) Theoretical Approaches to X-ray Absorption Fine

642   Structure. Reviews of Modern Physics, 72, 621.

643

644   Rohrbach, A. and Schmidt, M. W. (2011) Redox freezing and melting in the Earth's

645   deep mantle resulting from carbon-iron redox coupling. Nature 472, 209–212.

646

647   Saunders, A.D. and Tarney, J. (1984) Geochemical characteristics of basaltic volcanism

648   within back-arc basins. Geological Society, London, Special Publications, 16, 59-76.

649

650   Smith, D., Lawler, K.V., Martinez-Canales, M., Daykin, A.W., Fussell, Z., Smith,

651   G.A., Childs, C., Smith, J.S., Pickard, C.J., and Salamat, A. (2018) Postaragonite phases

652   of $CaCO_3$ at lower mantle pressures. Physical Review Materials, 2, 013605.

653

654   Solomatova, N.V. and Asimow, P.D. (2017) Ab initio study of the structure and

655   stability of $CaMg(CO_3)_2$ at high pressure. American Mineralogist, 102, 210-215.

656

657   Stagno, V., Tange, Y., Miyajima, N., McCammon, C.A., Irifune, T., and Frost, D.J.

658   (2011) The stability of magnesite in the transition zone and lower mantle as function of

659   oxygen fugacity. Geophysical Research Letters, 38, L19309.

660

661   Syracuse, E.M., van Keken, P.E., and Abers, G.A. (2010) The global range of

662   subduction zone thermal models. Physics of the Earth and Planetary Interiors, 183, 73-

663   90.

664

665   Takley, P.J., Stevenson, D.J., Glatzmaier, G.A. and Schubert, G. (1993) Effects of an

666   endothermic phase transition at 670 km depth in a spherical model of convection in the

667   Earth's mantle. Nature, 361, 699-703.

668

669   Tao, R., Fei, Y., and Zhang, L. (2013) Experimental determination of siderite stability

670   at high pressure. American Mineralogist, 98, 1565-1572.

671

672   Thomson, A.R., Walter, M.J., Kohn, S.C., and Brooker, R.A. (2015) Slab melting as a

673   barrier to deep carbon subduction. Nature, 529, 76-79.

674

675   Walter, M.J., Kohn, S.C., Araujo, D., Bulanova, G.P., Smith, C.B., Gaillou, E., Wang,

676   J., Steele, A., and Shirey, S.B. (2011) Deep Mantle Cycling of Oceanic Crust: Evidence

677   from Diamonds and Their Mineral Inclusions. Science, 334, 54-57.

678

679   Westre, T. E., Kennepohl, P., DeWitt, J. G., Hedman, B., Hodgson, K. O., and

680   Solomon, O. E. (1997) A Multiplet Analysis of Fe K-Edge 1s → 3d Pre-Edge Features

681   of Iron Complexes. Journal of the American Chemical Society, 119, 6297-6314.

682

683   Wilke, M., Farges, F., Petit, P.E., Brown, Jr. G.E., and Martin, F. (2001) Oxidation state

684   and coordination of Fe in minerals: an Fe K XANES spectroscopic study. American

685   Mineralogist, 86, 714-730.

686

687   Wilke, M., Farges, F., Partzsch, G.M., Schmidt, C., and Behrens, H. (2007) Speciation

688   of iron in silicate glasses and melts by in-situ XANES spectroscopy. American

689   Mineralogist, 92, 44-56.

690

691   Zhao, D. (2003) Global tomographic images of mantle plumes and subducting slabs:

692   insight into deep Earth dynamics. Physics of the Earth and Planetary Interiors, 146, 3-

693   34.

694

Table 1. Details of crystal structure of synthetic $FeCO_3$ and $HP-Fe_3O_4$ single crystal at different pressures and ambient temperature and atomic coordinates used for simulations

Sample	P (GPa)	a	b	c	vol	α	β	γ
FeCO$_3$	4(1)	4.661(1)	/	15.09(5)	283.8(4)	90	90	120
(R 3 c,	37(1)	4.530(4)	/	13.46(19)	239.2(3)	90	90	120
Z = 6)	55(1)	4.346(1)	/	12.4(4)	202.8(2)	90	90	120
HP-Fe$_3$O$_4$								
(Bbmm,	51(1)	9.230(13)	9.168(4)	2.6775(12)	226.6(3)	90	90	90
Z = 4)								

FeCO$_3$ - 4(1) GPa				FeCO$_3$ - 37(1) GPa			
Site	x	y	z	Site	x	y	z
Fe	0.0000	0.0000	0.0000	Fe	0.0000	0.0000	0.0000
C	0.0000	0.0000	0.2500	C	0.0000	0.0000	0.2500
O	0.27525	0.0000	0.2500	O	0.27912	0.0000	0.2500

FeCO$_3$ - 55(1) GPa				HP-Fe$_3$O$_4$ - 51(1) GPa			
Site	x	y	z	Site	x	y	z
Fe	0.0000	0.0000	0.0000	Fe(1)	0.1328	0.0744	0.0000
C	0.0000	0.0000	0.2500	Fe(2)	0.3809	0.2500	0.0000
O	0.2895	0.0000	0.2500	O(1)	0.5000	0.0000	0.0000
				O(2)	0.0300	0.2500	0.0000
				O(3)	0.2210	-0.1176	0.0000

695

21

696

697   **Figure 1**
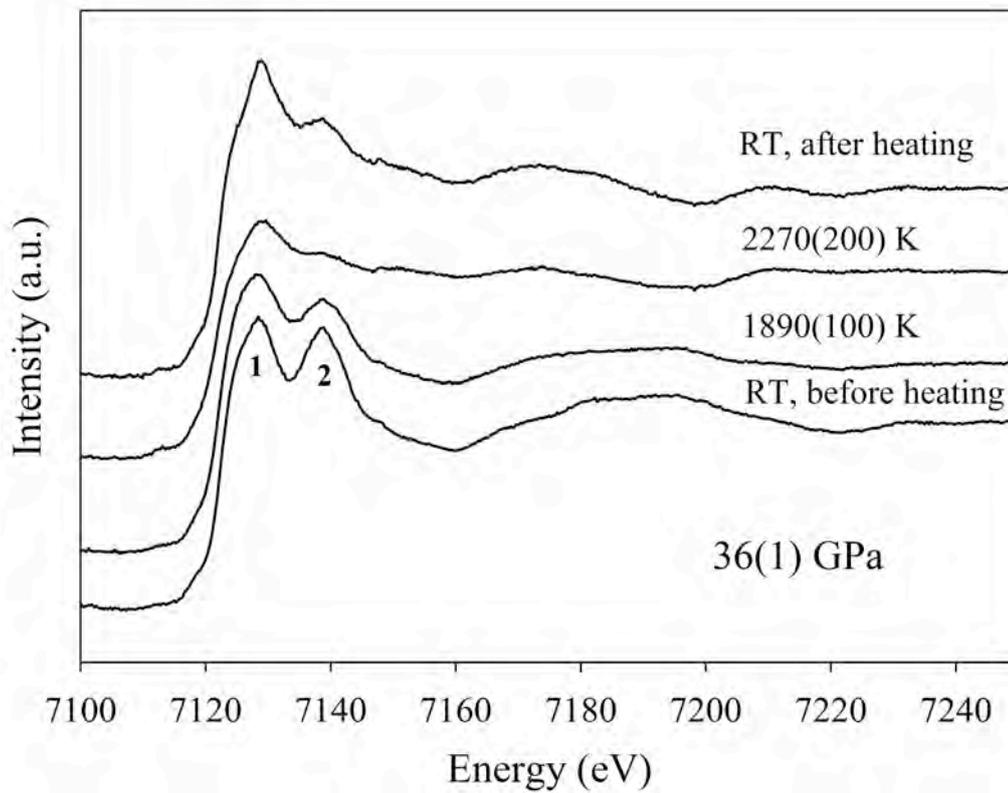
698

699

700   **Figure 2**

**Figure 3**

Figure 4

23
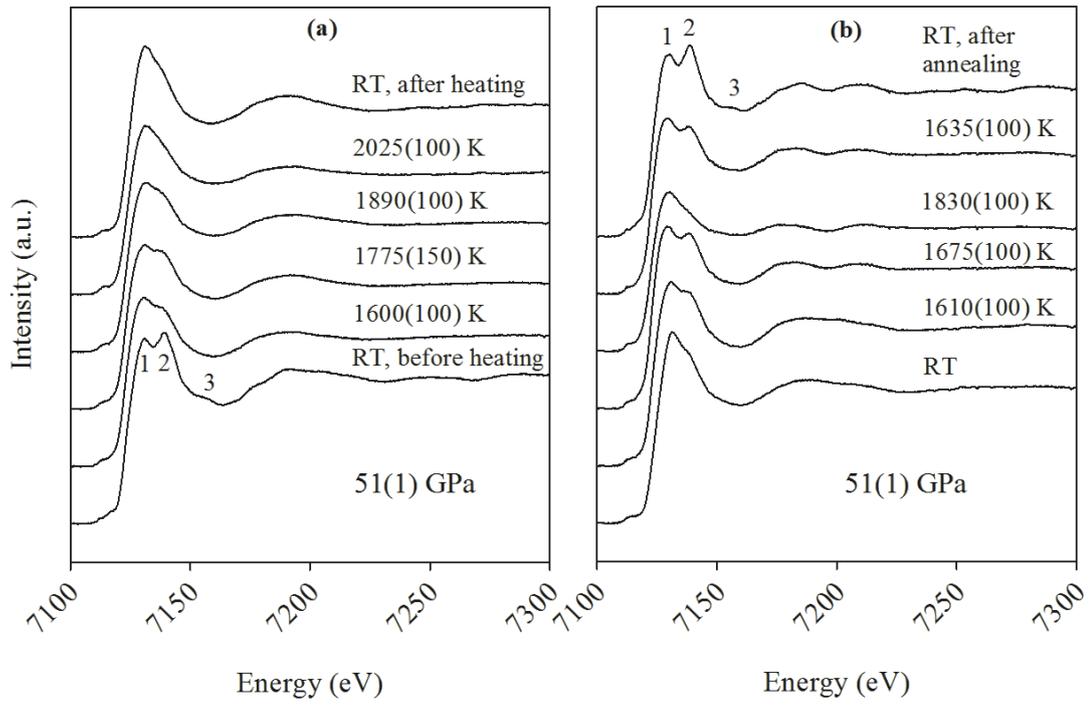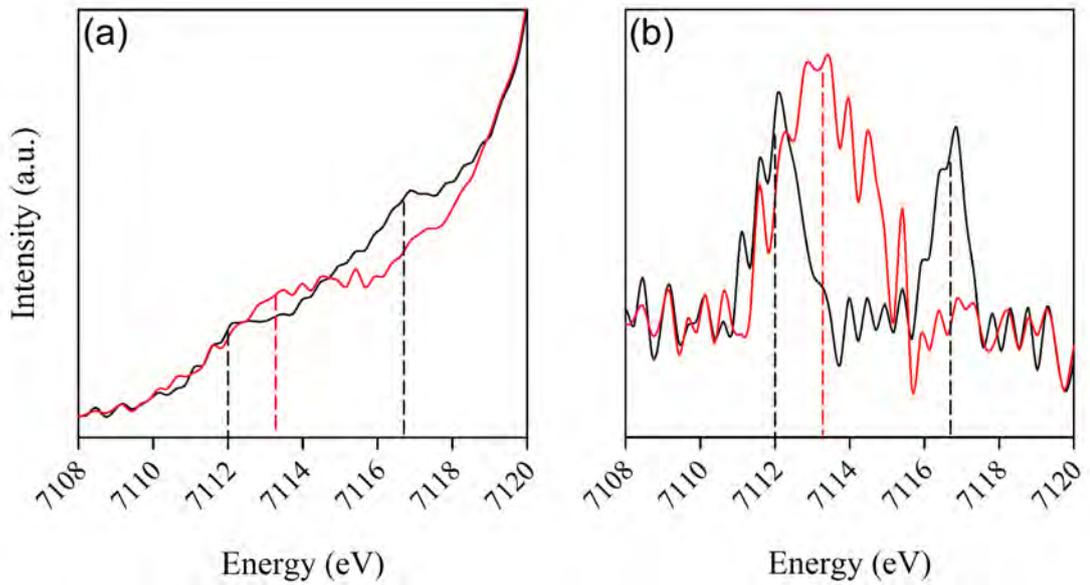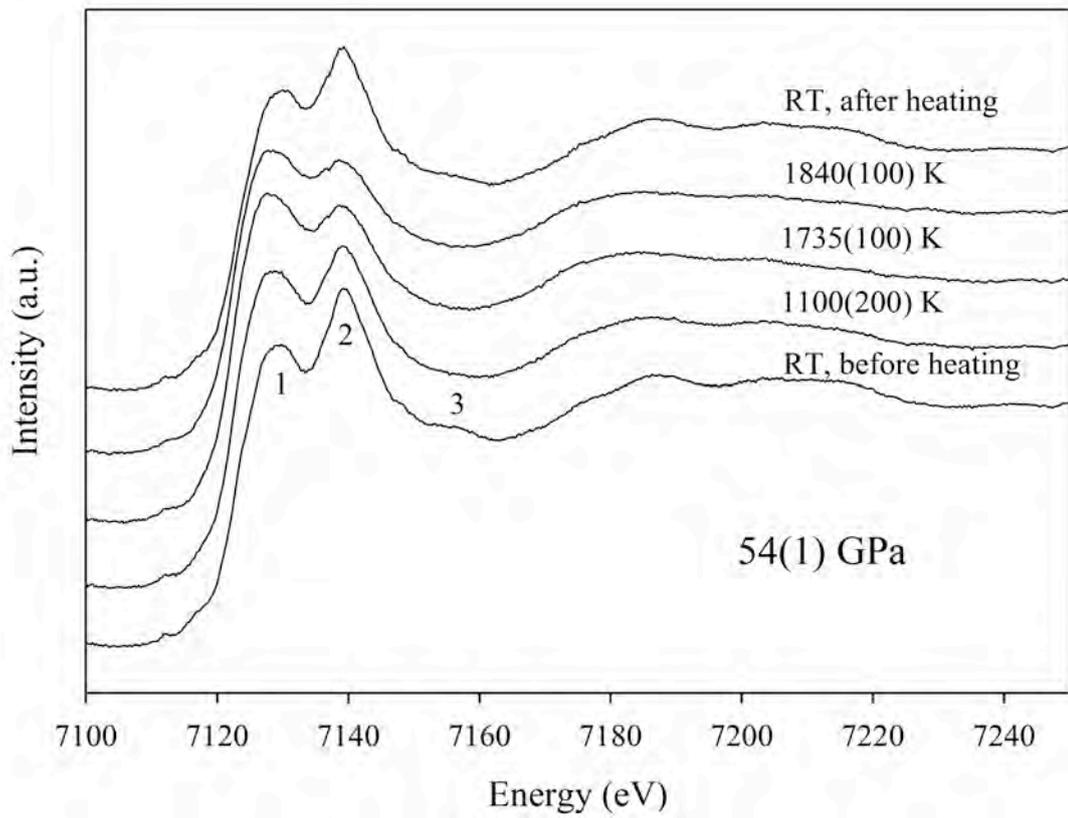
707

708

709   **Figure 5**
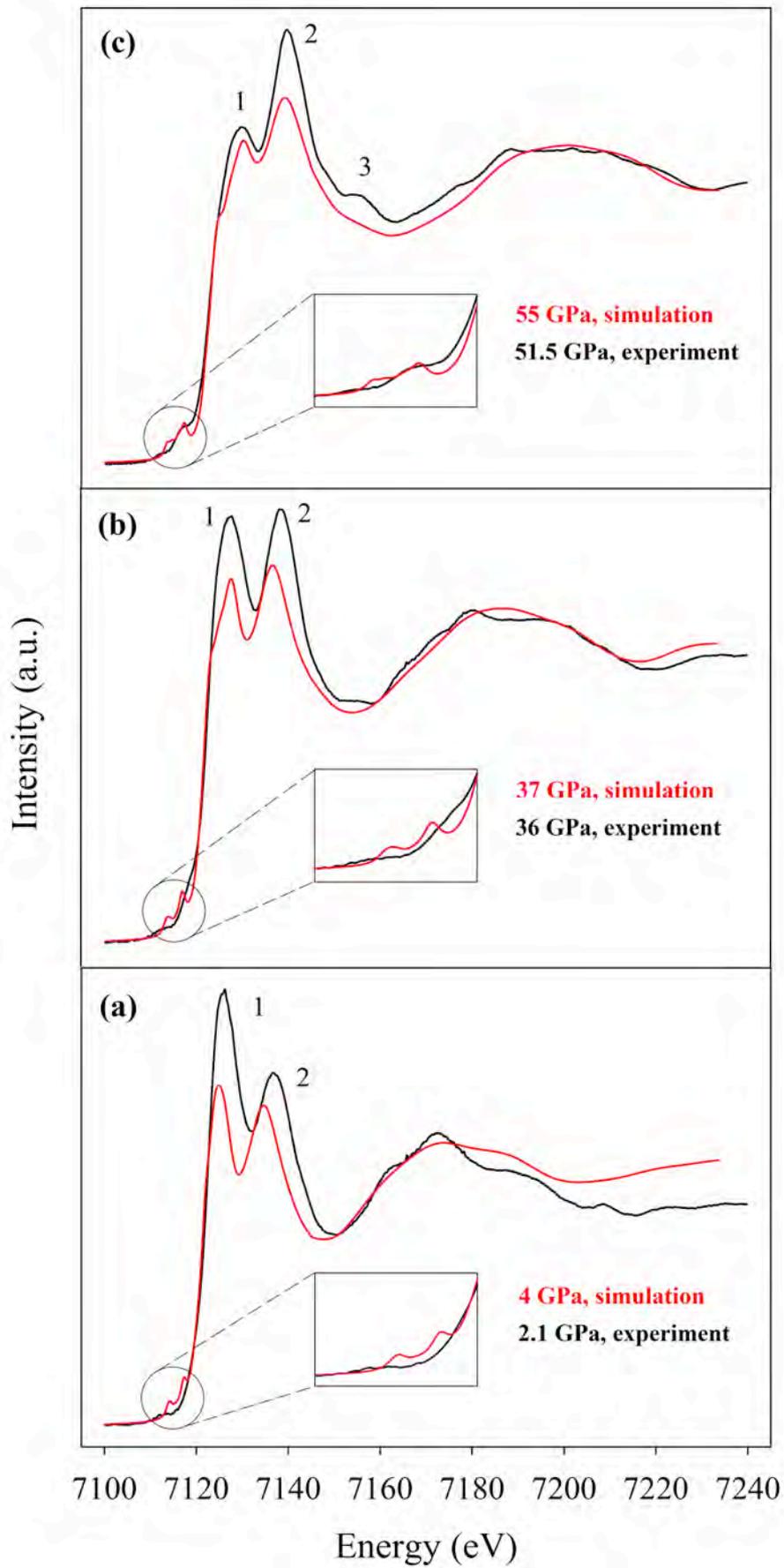
710

25

711   **Figure 6**

712
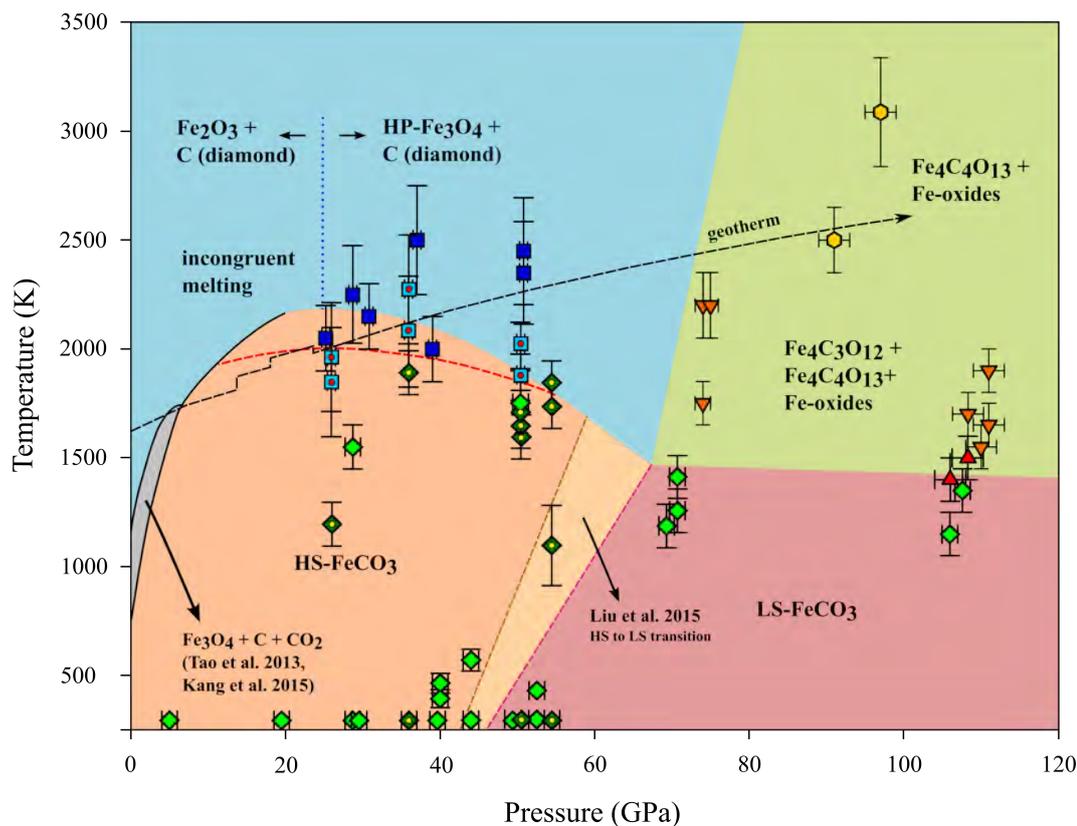
713

714

715   **Figure 7**
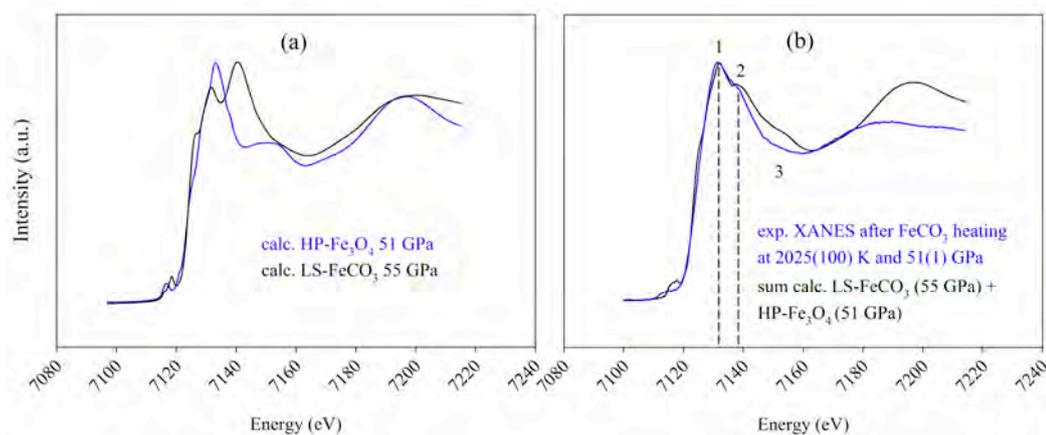
716

717

718   **Figures caption**

719   **Figure 1.** Experimental normalized XANES spectra of the Fe-K edge of $FeCO_3$ at 36(1)

720   GPa and measured *in situ* at the indicated temperatures. Peaks marked "1" and "2" are

721   characteristic for $FeCO_3$ and are used to monitor the state of the material. After heating

722   at 2270(200) K the spectra radically change, indicating chemical and/or physical

723   changes in the system.

724

725   **Figure 2.** Experimental normalized $FeCO_3$ XANES spectra at 51(1) GPa and measured

726   *in situ* at the indicated temperatures. (a) At room temperature, features characteristic of

727   low-spin $FeCO_3$ (including the peak marked "3"; Cerantola et al. 2015) are visible.

728   Increasing temperature stabilizes the high-spin state (marked by the intensity exchange

729   of peaks 1 and 2 and the disappearance of peak 3), but above 1775(150) K the spectra

730   change more drastically. (b) Annealing of the run product(s) at moderate temperatures

731   shows nearly full recovery of the original spectrum after annealing but with two new

732   humps at ~7185 and ~7210 eV.

733

734   **Figure 3.** Expanded view of the pre-edge region of ambient temperature spectra at

735   51(1) GPa (a) normalized and (b) normalized with background subtracted. The black

736   solid line shows the spectrum before heating (Fig. 2a bottom) and the red solid line

737   shows the spectrum after quenching from 2025(100) K (Fig. 2a top). The black curve

738   shows a pre-edge at ~7112 eV and a sharp feature at ~7116.5 eV, which matches well

739   with the pre-edge region in low-spin $FeCO_3$ (see Cerantola et al. 2015). The red curve

740   has one broad hump at ~7113.5 eV that dominates the spectrum, indicating the presence

741   of one or more Fe-containing phase(s). Note that both pre-edges in Fig. 3b were

742   normalized following the same background subtraction procedure.

743

744   **Figure 4.** Experimental normalized $FeCO_3$ XANES spectra at 54(1) GPa and measured

745   *in situ* at the indicated temperatures. With increasing temperature at constant pressure,

746   iron atoms undergo a low-spin to high-spin transition, marked by a change in relative

747   intensity of peaks 1 and 2 and disappearance of peak 3 (Cerantola et al. 2015). There is

748   no signature indicative of decomposition reactions, and the spectrum after quenching

749   matches closely to the spectrum before heating.

750

751   **Figure 5.** Experimental (black) and simulated (red) XANES spectra of $FeCO_3$ at

752   different pressures. The insets magnify the pre-edge region. (a) Spectra show features

753   characteristic of $FeCO_3$ in the high-spin state, where peak 1 is more intense than peak

754   2 and peak 3 is absent. Note that the pre-edge in the calculated spectrum is at 7117 eV,

27

755   5 eV higher than in the experimental spectrum, with a lower intensity feature at 7113.5

756   eV. (b) Spectra are characteristic for high-spin $FeCO_3$ just before spin crossover, where

757   peak 2 is slightly more intense than peak 1. In the experimental spectrum a new feature

758   appears at ~7116.5 eV, whereas the simulated spectrum has a pre-edge at 7117 eV and

759   the same broad low intensity feature at ~7113.5 eV. (c) After iron spin crossover, peak

760   2 is more intense than peak 1 and peak 3 appears in the experimental spectrum at ~7155

761   eV. Analogous to spectra at 37 GPa, the pre-edge peak in the calculated spectrum is at

762   higher energy than in the experimental spectrum. The broad feature at ~7113.5 eV

763   becomes slightly more pronounced. Note the absence of peak 3 in the calculated

764   spectrum. The onset energy of each calculated spectrum was adjusted according to the

765   variation in the Fermi energy and in the s core level energy shift.

766

767   **Figure 6.** Updated stability diagram of $FeCO_3$ at high pressure and high temperature

768   (modified from Cerantola et al. 2017). Symbols from this study are: dark green

769   diamonds with yellow dot - $FeCO_3$; light blue squares with red dot - oxide(s) and

770   recrystallized $FeCO_3$;. Symbols from Cerantola et al. (2017) are: light green diamonds

771   - $FeCO_3$; blue squares - oxide(s) and recrystallized $FeCO_3$; red triangles - tetrairon (III)

772   orthocarbonate $Fe_4C_3O_{12}$; orange inverse triangles - diiron (II) diiron (III)

773   tetracarbonate $Fe_4C_4O_{13}$ + $Fe_4C_3O_{12}$ + oxide(s); yellow hexagons - $Fe_4C_4O_{13}$ + oxides.

774   The shading is as follows: grey region - $FeCO_3$ decomposition to Fe_3O_4 + C + CO_2 (Tao

775   et al. 2013; Kang et al. 2015); orange region - high-spin $FeCO_3$, red region - low-spin

776    $FeCO_3$ (Liu et al. 2015); blue region - melting of $FeCO_3$; green region - formation of

777   high-pressure carbonates $Fe_4C_3O_{12}$ and $Fe_4C_4O_{13}$ (Cerantola et al. 2017). Black dashed

778   curve - expected mantle geotherm (Katsura et al. 2010); thick red dashed line - new

779   boundary proposed in this study between crystalline $FeCO_3$ and incongruent melt;

780   brown and violet dashed lines - spin transition region in magnesio-siderite from Liu et

781   al. 2015 and consistent with Müller et al. 2017. A vertical dotted blue line separates the

782   regions in which the formation of α- Fe_2O_3 and HP-Fe_3O_4 was observed upon melting

783   of $FeCO_3$.

784

785   **Figure 7.** (a) Comparison between calculated XANES spectra of LS-$FeCO_3$ (black)

786   and HP-Fe_3O_4 (blue). (b) Comparison between the sum of HP-Fe_3O_4 and LS-$FeCO_3$

787   calculated spectra (see Fig. 7a) (black) and the experimental spectrum after heating

788    $FeCO_3$ at 2025(100) K (blue). The presence of recrystallized HP-Fe_3O_4 after $FeCO_3$

789   (partial) melting at 51(1) was already observed using SXRD by Cerantola et al. 2017.

790   The presence of other Fe-oxide phases cannot be excluded.